Polyoxometalate-based metal-organic frameworks for boosting electrochemical capacitor performance

Dongfeng Chai, Carlos J. Gómez-García, Bonan Li, Haijun Pang, Huiyuan Ma, Xinming Wang, Lichao Tan

PII: S1385-8947(19)31108-8
DOI: https://doi.org/10.1016/j.cej.2019.05.084
Reference: CEJ 21723

To appear in: *Chemical Engineering Journal*

Received Date: 23 February 2019
Revised Date: 11 May 2019
Accepted Date: 14 May 2019

Please cite this article as: D. Chai, C.J. Gómez-García, B. Li, H. Pang, H. Ma, X. Wang, L. Tan, Polyoxometalate-based metal-organic frameworks for boosting electrochemical capacitor performance, *Chemical Engineering Journal* (2019), doi: https://doi.org/10.1016/j.cej.2019.05.084

Polyoxometalate-based metal-organic frameworks for boosting electrochemical capacitor performance

Dongfeng Chai[a], Carlos J. Gómez-García[b], Bonan Li[a], Haijun Pang[a,*], Huiyuan Ma[a,*], Xinming Wang[a], Lichao Tan[a]

[a]School of Materials Science and Engineering, College of Chemical and Environmental Engineering, Harbin University of Science and Technology, Harbin 150040, P. R. China. E-mail address: panghj116@163.com, mahy017@163.com.

[b]Instituto de Ciencia Molecular, Departamento de Química Inorgánica. Universidad de Valencia. C/Catedrático José Beltrán, 2. 46980 Paterna, Spain

Keywords: polyoxometalate, polyoxometalate-based metal-organic framework, single active site, *pseudo*-rotaxane, oxidation capacity, electrochemical capacitor

Abstract

Polyoxometalate-based metal-organic frameworks (POMOFs) possess promising applications as capacitors. Herein, we report the syntheses, structures and electrochemical properties of five copper-containing POMOFs: $[Cu^{I}_4H_2(btx)_5(PW_{12}O_{40})_2]\cdot 2H_2O$ (**1**), $[Cu^{II}Cu^{I}_3(H_2O)_2(btx)_5(PW^{VI}_{10}W^{V}_2O_{40})]\cdot 2H_2O$ (**2**), $[Cu^{I}_6(btx)_6(PW^{VI}_9W^{V}_3O_{40})]\cdot 2H_2O$ (**3**), $[Cu^{I}_4H_2(btx)_5(PMo_{12}O_{40})_2]\cdot 2H_2O$ (**4**) and $[Cu^{II}Cu^{I}_3(btx)_5(SiMo^{VI}_{11}Mo^{V}O_{40})]\cdot 4H_2O$ (**5**) (btx = 1,4-bis(triazol-1-ylmethyl) benzene) with potential applications as capacitors. Compounds **1**-**3** contain the same Keggin-type polyoxometalate (POM) although with different oxidation states, allowing the analysis of the effect of the electronic population on the capacitance performance of this Keggin-type POM. Compounds **1**/**4** and **2**/**5** present the same microstructure but different chemical composition, allowing the analysis of the effect of the chemical composition on the

capacitance performance of these isostructure POMOFs. Compound **4** shows the highest specific capacitance (237.0 F g^{-1} at 2 A g^{-1}) with capacitance retention of about 92.5 % after 1000 cycles at a high charge/discharge current density of 10 A g^{-1}. Such superior performance is comparable with state-of-the-art MOF-based and POM-based supercapacitor electrode materials. More important, this work demonstrates that the design and syntheses of POMOFs by tuning single active site (SAS) could guide the development of the new generation of electrode materials for electrochemical capacitors in the near future.

1. Introduction

The search of new materials for energy storage is a very hot topic nowadays due to the current and previsible future evolution of the world energy demand.[1-11] Generally, the specific capacitance of pseudocapacitors may be 10 to 100 times higher than EDLCs.[12] RuO_2 is a gold-standard of pseudocapacitor material because its fast and reversible multi-electron transfer reactions with overlapping peak potentials.[13, 14] Recently, polyoxometalates (POMs) have been suggested as an alternative to replace RuO_2 due to their low-cost and unique redox activities.[15-17] In addition, POMs may act as electron reservoirs or sponges and exhibit a rich structural versatility and excellent electrochemical properties.[14, 18-22] One of the most promising POMs is the classic α-Keggin-type structure ($[XM_{12}O_{40}]^{n-}$ or XM_{12}) since it presents very interesting charge/recharge properties.[23-26] For example, phosphotungstate (PW_{12}) can be used as cathode for boosting rechargeable lithium ion batteries.[24] Phosphomolybdate (PMo_{12}) exhibits a 24-electron reduction in the discharging processes with a large theoretical capacity of about 270 mA h g^{-1}, higher than the commercial cathode Li_2CoO_2 (140 mA h g^{-1}).[25, 26] However, their high solubility in most solvents or electrolytes impedes their applications as solid-state electrode materials. To solve this problem, POMs have been inserted into two

different kinds of matrices: conducting polymers and carbon materials.[16, 27-43] Nevertheless, none of these methods take advantage of the rich and adjustable structural diversity of POMs. A very promising, although less used strategy, is the immobilization of POMs in metal-organic frameworks (MOFs) since they exhibit high specific surface areas, adjustable pores, open and ordered metal sites and have been used for electrochemical capacitors.[44-70] We have innovatively used this strategy to immobilize POMs on MOFs to build novel crystalline POMOFs with potential applications as supercapacitors.[71-73] Integrating POMs within MOFs to construct stable and versatile POMOFs with an unprecedented degree of structural precision could solve the problem of the high solubility of POMs in most solvents or electrolytes and enhance the electrical conductivity thanks to the multi-dimensional networks. Additionally, the active sites of the crystalline structures of POMOFs are homogeneous and well ordered, which an advantage is easily tuned to explore reaction mechanism.[74] Albeit, to the best of our knowledge, the relationship between electrochemical capacitor performance and structure of these POMOFs is not fully understood and tuning single active site (SAS) in crystalline POMOFs for boosting their electrochemical capacitor performance is not deeply explored.

Inspired by the above analysis, we have successfully synthesized five new POMOFs based on *α*-Keggin POMs with different Cu(II) and Cu(I) complexes with the ligand btx (1,4-bis(triazol-1-ylmethyl)benzene). These five POMOFs are: $[Cu^{I}_4H_2(btx)_5(PW_{12}O_{40})_2]\cdot 2H_2O$ (**1**), $[Cu^{II}Cu^{I}_3(H_2O)_2(btx)_5(PW^{VI}_{10}W^{V}_2O_{40})]\cdot 2H_2O$ (**2**), $[Cu^{I}_6(btx)_6(PW^{VI}_9W^{V}_3O_{40})]\cdot 2H_2O$ (**3**), $[Cu^{I}_4H_2(btx)_5(PMo_{12}O_{40})_2]\cdot 2H_2O$ (**4**) and $[Cu^{II}Cu^{I}_3(btx)_5(SiMo^{VI}_{11}Mo^{V}O_{40})]\cdot 4H_2O$ (**5**). Compounds **1**-**3** have the same PW_{12} Keegin POM although with different oxidation states of the W atom and, accordingly, with different global charges (-3 in **1**, -5 in **2** and -6 in **3**). This series allow the study of the influence of the oxidation state of the metal ions of the POM on the

capacitance performance. Compounds **1** and **4** as well as compounds **2** and **5** are two pairs of isostructural compounds that only differ in the metal atom of the Keggin POM (W in **1** and **2** *vs*. Mo in **4** and **5**). These two couples of isostructural compounds allow the study of the influence of the metal atom (W or Mo) in the capacitance performance of these POMOFs. To some extent, these series of POMOFs with defined single crystal structures not only realize SAS tuning, but also provide a good opportunity to explore the relationship between electrochemical capacitor performance and structures of these POMOFs.

2. Results and discussion

Single crystal X-ray diffraction analyses reveal that all of the compounds contain α-Keggin POMs, copper ions, btx ligands and crystallization water molecules (Figures S1 to S4). CCDC-1864234(**1**), CCDC-1864235(**2**), CCDC-1864236(**3**), CCDC-1864237 (**4**) and CCDC-1864238 (**5**) contain supplementary crystallographic data for these compounds. Crystal data and structure refinements for the five compounds are listed in Table S1. Selected bonds lengths (Å) and angles (°) for the five compounds are listed in Tables S2 to S6.

2.1 Structure of compounds $[Cu^{I}_{4}H_{2}(btx)_{5}(PW_{12}O_{40})_{2}]\cdot 2H_{2}O$ (1) and $[Cu^{I}_{4}H_{2}(btx)_{5}(PMo_{12}O_{40})_{2}]\cdot 2H_{2}O$ (4). Compounds **1** and **4** are isostructural, and both of them crystallize in the triclinic space group *P*-1 (No. 2). Therefore, only the structure of **1** is described in detail. Compound **1** consists of $[PW_{12}O_{40}]^{3-}$ polyoxoanions (PW_{12}), Cu-btx chains and free btx ligands.

The PW_{12} polyoxoanions present the α-Keggin structure and connect two neighbouring Cu-btx chains (Figure 1a). The central P atom is surrounded by a cube of eight disordered O atoms resulting from the superposition of two PO_4 tetrahedra with an occupancy factor of ½, as has been observed in previous compounds[75] and in many salts containing weakly polarizing

cations as decamethylferrocene ($Fe(C_5Me_5)_2$),[76] bis(ethylendithio)-tetrathiafulvalene (BEDT-TTF),[77-80] bis(ethylenethio) tetrathiafulvalene (BET-TTF)[81] and bis(ethylenediseleno)tetrathiafulvalene (BEDS-TTF).[82] The Cu(I) atoms are tri-coordinated by two btx ligands and a PW_{12} polyoxoanion forming a T-shape coordination geometry (Figure 1b). The PW_{12} anions connecting consecutive Cu-btx chains generate macrocycles formed by two POM, six Cu(I) ions and four bridging btx ligands (POM_2-Cu_6-btx_4, Figure 1a). Adjacent POM_2-Cu_6-btx_4 macrocycles are fused *via* the PW_{12} anions and Cu-btx chains to give rise to brick-wall like 2D-lattice layers, as shown in Figure 1b. These 2D-lattice layers are stacked in an alternating way following an …ABC… sequence (Figures 1c and 1d). The free btx ligands connect adjacent layers *via* several hydrogen bond interactions (O5···O18 = 2.862 Å, O6···O19 = 2.944 Å, N14···O33 = 3.000 Å and N9···N13 = 3.065 Å), providing a further stabilization for the alternating packing.

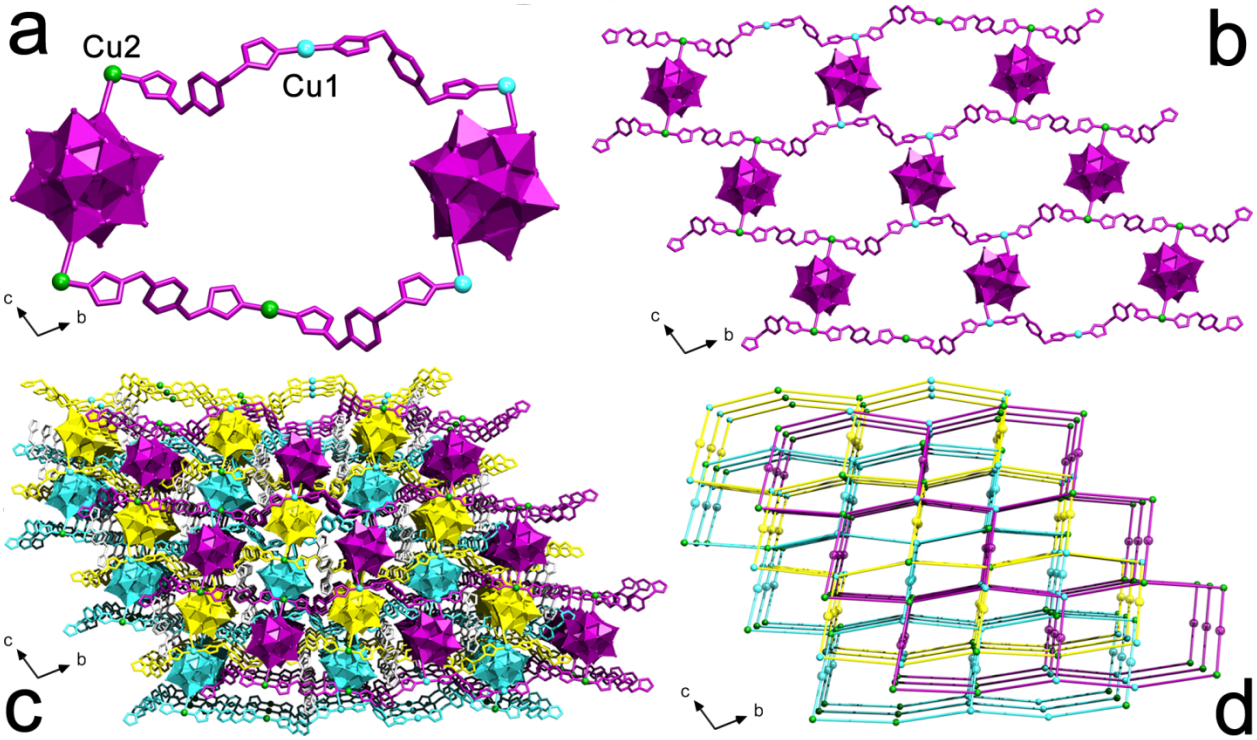

Figure 1. *Structure of compound* ***1*** *(similar to* ***4****):* ***(a)*** *The POM$_2$-Cu$_6$-btx$_4$ macrocycle.* ***(b)*** *View of a fragment of the brick-wall like 2D-lattice layer.* ***(c)*** *Packing of the alternating layers (A, B and C type layers are depicted in purple, blue and yellow).* ***(d)*** *Schematic view of the packed layers showing the positions of Cu(I) ions (small spheres) and POMs (big spheres).*

2.2 Structure of compounds $[Cu^{II}Cu^{I}_3(H_2O)_2(btx)_5(PW^{VI}_{10}W^{V}_2O_{40})]\cdot 2H_2O$ (2) and $[Cu^{II}Cu^{I}_3(btx)_5(SiMo^{VI}_{11}Mo^{V}O_{40})]\cdot 4H_2O$ (5). Single crystal X-ray diffraction analyses reveal that compounds **2** and **5** are isostructural, and both of them crystallize in the triclinic space group *P*-1 (No. 2). Therefore, only the structure of **5** is described in detail.

The formula unit contains four different Cu atoms (Cu1-Cu4), one $[SiMo^{VI}_{11}Mo^{V}O_{40}]^{5-}$ polyoxoanion and five btx ligands. There are three Cu(I) (Cu2, Cu3 and Cu4) and one Cu(II) (Cu1) ions per formula unit that compensate the -5 charge of the $[SiMo^{VI}_{11}Mo^{V}O_{40}]^{5-}$ polyoxoanion $(SiMo_{12})^{5-}$. Compounds **5** shows an unusual 1D + 3D structure consisting of zigzag chains (made of Cu4 and btx ligands) inserted in the channels of a 3D covalent framework formed by the Keggin-type $(SiMo_{12})^{5-}$ polyoxoanions, copper ions and btx ligands (Figure 2). The 3D covalent framework is built by 2D rectangular layers containing Cu1 and Cu2 ions connected through btx ligands (Figure 2a), by 1D chains containing Cu3 ions connected through btx ligands (Figure 2a) and by $(SiMo_{12})^{5-}$ coordinating with three types of Cu ions through bridging oxygen and terminal oxygen atoms (Figure 2b). The $(SiMo_{12})^{5-}$ polyoxoanions occupy the cavities formed by 2D rectangular layers and 1D chains. Cu1 is hexa-coordinated to four btx ligands and two $(SiMo_{12})^{5-}$ through two terminal oxygen atoms of the POM. Cu2 is tetra-coordinated to two btx ligands and two $(SiMo_{12})^{5-}$ through two bridging oxygen atoms of the POM. Cu3 is hexa-coordinated to two btx ligands and two $SiMo_{12}$ through two terminal and two bridging oxygen atoms of the POM. Finally, Cu4 is coordinated to only two N atoms from

two btx ligands forming the Cu4-btx chain. Each $SiMo_{12}$ polyoxoanion is connected to a total of six Cu ions (two Cu1, two Cu2 and two Cu3, Figure 2b), to build a 3D framework including generating {Cu1-btx-Cu2-POM} macrocycles (Figure S5) that act as molecular "loops" that are threaded by the Cu4-btx chains acting as molecular "strings" to form an unusual 1D + 3D *pseudo*-rotaxane structure, as shown in Figures 2c and 2d.

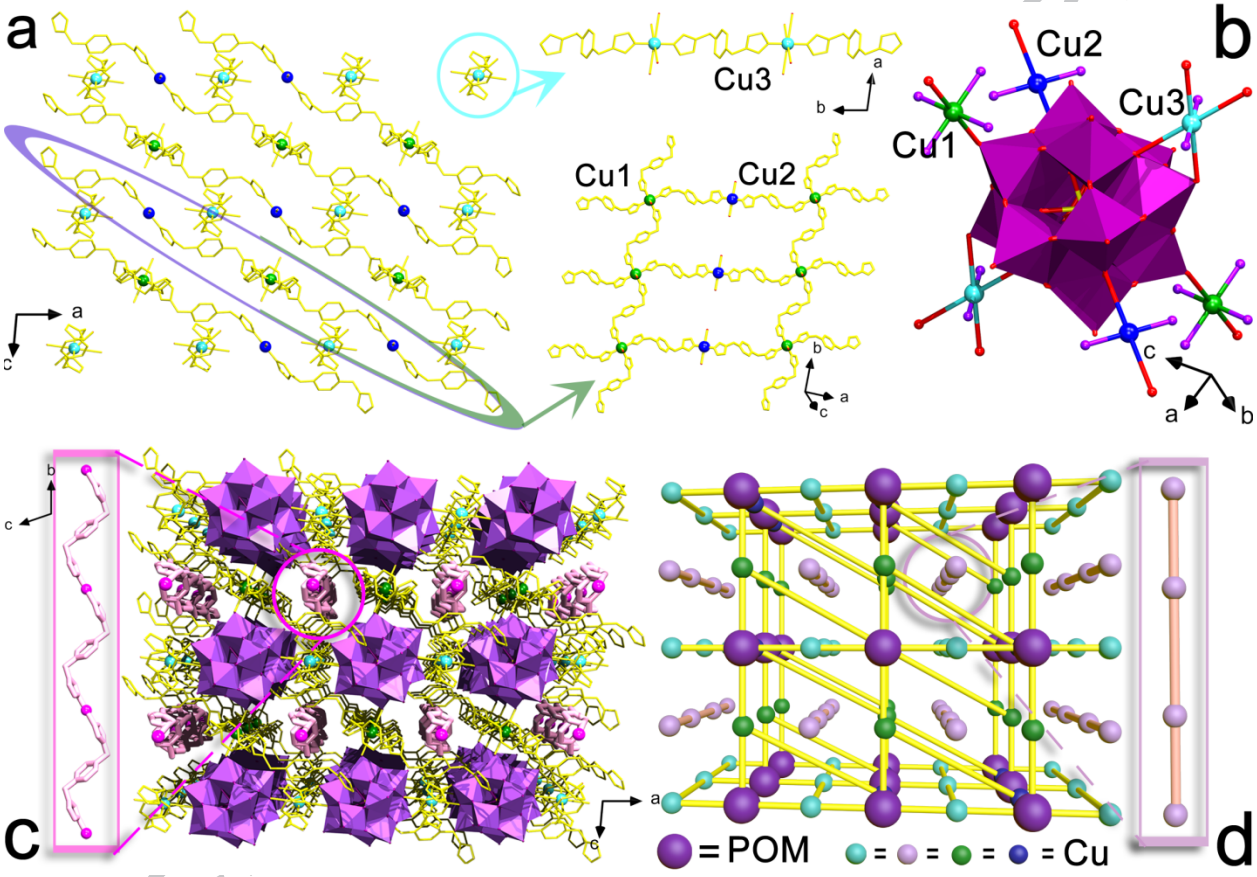

Figure 2. *Structure of compound* ***5*** *(similar to* ***2****):* ***(a)*** *The Cu1-btx-Cu2 2D rectangular layers and the Cu3-btx 1D chains;* ***(b)*** *The hexa-connected* $(SiMo_{12})^{5-}$ *polyoxoanion;* ***(c)*** *and* ***(d)*** *The 1D + 3D pseudo-rotaxane structure. Purple polyhedrons/big spheres represent the polyoxoanions, small spheres represent the Cu atoms and the yellow sticks represent the btx ligands.*

2.3 Structure of compound $[Cu^{I}_{6}(btx)_{6}(PW^{VI}_{9}W^{V}_{3}O_{40})]\cdot 2H_2O$ (3). The single crystal X-ray diffraction analysis reveals that compound **3** crystallizes in the triclinic space group *P*1 (No. 1). Compound **3** shows a 3D POMOF structure formed by Keggin $[PW^{VI}_{9}W^{V}_{3}O_{40}]^{6-}$ polyoxoanions $(PW_{12})^{6-}$, Cu(I) atoms and btx ligands. The POMOF structure can be considered as a 3D open framework with inserted oblique Cu2-btx-Cu3 layers that further connect the $(PW_{12})^{6-}$ polyoxoanions. The layers are formed by Cu2 and Cu3 atoms connected by btx ligands that are further connected to the $(PW_{12})^{6-}$ polyoxoanions. Each POM is connected to two Cu2 and two Cu3 ions (Figure S6) belonging to two different layers and therefore each POM connects two parallel oblique layers giving rise to a double Cu-btx layer (Figure 3a).

The 3D framework is formed by square POM/Cu1 lattices which are further connected by btx ligands through Cu1-btx-Cu1 bridges to generate a 3D lattice (Figures 3b and S7). These POM/Cu1 square lattices contain POMs connected to four Cu1 atoms where each Cu1 atom is connected to two $(PW_{12})^{6-}$ polyoxoanions along the *a* axis, and to two btx ligands along the *b* and *c* axes, giving rise to a 3D open network as shown in Figures 3b and S7. Finally, the above described Cu2-btx-Cu3 layers are inserted in the 3D open framework to generate a more complicated 3D POMOF, as shown in Figures 3c and 3d. In the final 3D POMOF, the $(PW_{12})^{6-}$ polyoxoanions can be considered as high connectors since they are coordinated to two Cu2 atoms and two Cu3 atoms from the Cu2-btx-Cu3 layers and also to four Cu1 atoms from the 3D open framework, as shown in Figure S8.[83]

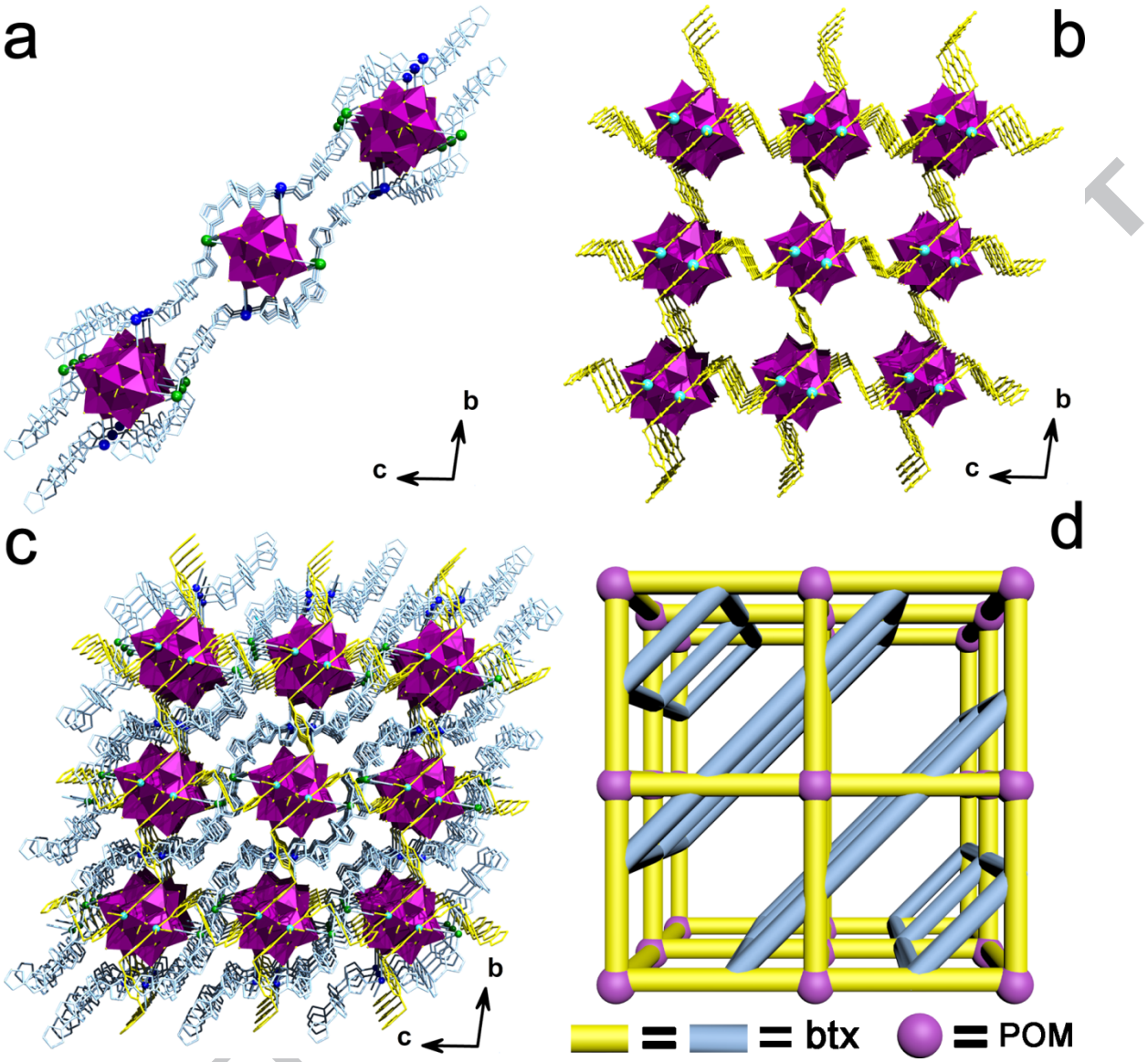

Figure 3. *Structure of compound* ***3*** *along a axis:* ***(a)*** *The oblique Cu2-btx-Cu3 layers consisting of* $(PW_{12})^{6-}$ *polyoxoanions, Cu2, Cu3 and btx ligands;* ***(b)*** *The 3D open framework formed by* $(PW_{12})^{6-}$ *polyoxoanions, Cu1 and btx ligands;* ***(c)*** *and* ***(d)*** *The complicated 3D POMOF formed by the 3D open framework (in yellow) with the inserted oblique Cu2-btx-Cu3 layers (in wathet).*

2.4 IR, XRPD and XPS analyses. The FT-IR spectrum test is an effective method to study the stability of electrode material. Herein, all the prepared compounds are immersed in the 1 M

H_2SO_4 solution for 0, 24, 48 and 96 h, then their FT-IR spectra are measured. The results that all the characteristic peaks in FT-IR spectra are nearly coincident from 0 to 96 h indicate the prepared compounds are stable, as shown in Figure S9. Additionally, to verify the phase purity of the compounds, the X-ray powder diffractograms (XRPD) of all the samples were measured before the test of capacitance properties. As expected, the diffraction peaks of both simulated and experimental patterns match well for all the samples (Figure S10), indicating a good phase purity of these compounds. Furthermore, we have performed X-ray photoemission spectra (XPS) of compounds **2**, **3** and **5** since part of the W and Mo atoms in these compounds should be reduced to the +5 oxidation state for charge balance. As shown in Figures 4a, 4c and 4e, the XPS spectra confirm that compounds **2** and **3** contain W, C, N, O and Cu, whereas compound **5** contains Mo, C, N, O and Cu. As shown in Figures 4b and 4d, the high-resolution W4f peaks are formed by the overlap of a few peaks. The fit of the curves gives the positions of these four peaks for **2** at about 35.4, 35.7, 37.6 and 37.9 eV, and at about 35.4, 35.9, 37.6 and 38.0 eV for **3**. These peaks are assigned to the $W^{V}4f_{7/2}$, $W^{VI}4f_{7/2}$, $W^{V}4f_{5/2}$ and $W^{VI}4f_{5/2}$, respectively.[84] The fit of the high-resolution Mo3d peaks gives the positions of four peaks for compound **5** at about 231.5, 232.8, 234.7 and 235.9 eV, which the four peaks correspond to $Mo^{V}3d_{5/2}$, $Mo^{VI}3d_{5/2}$, $Mo^{V}3d_{3/2}$ and $Mo^{VI}3d_{3/2}$, respectively, as shown in Figure 4f.[85] The results are consistent with the charge balance, indicating that the W^{VI} or Mo^{VI} atoms were partially reduced to W^{V} or Mo^{V} in compounds **2**, **3** and **5**.

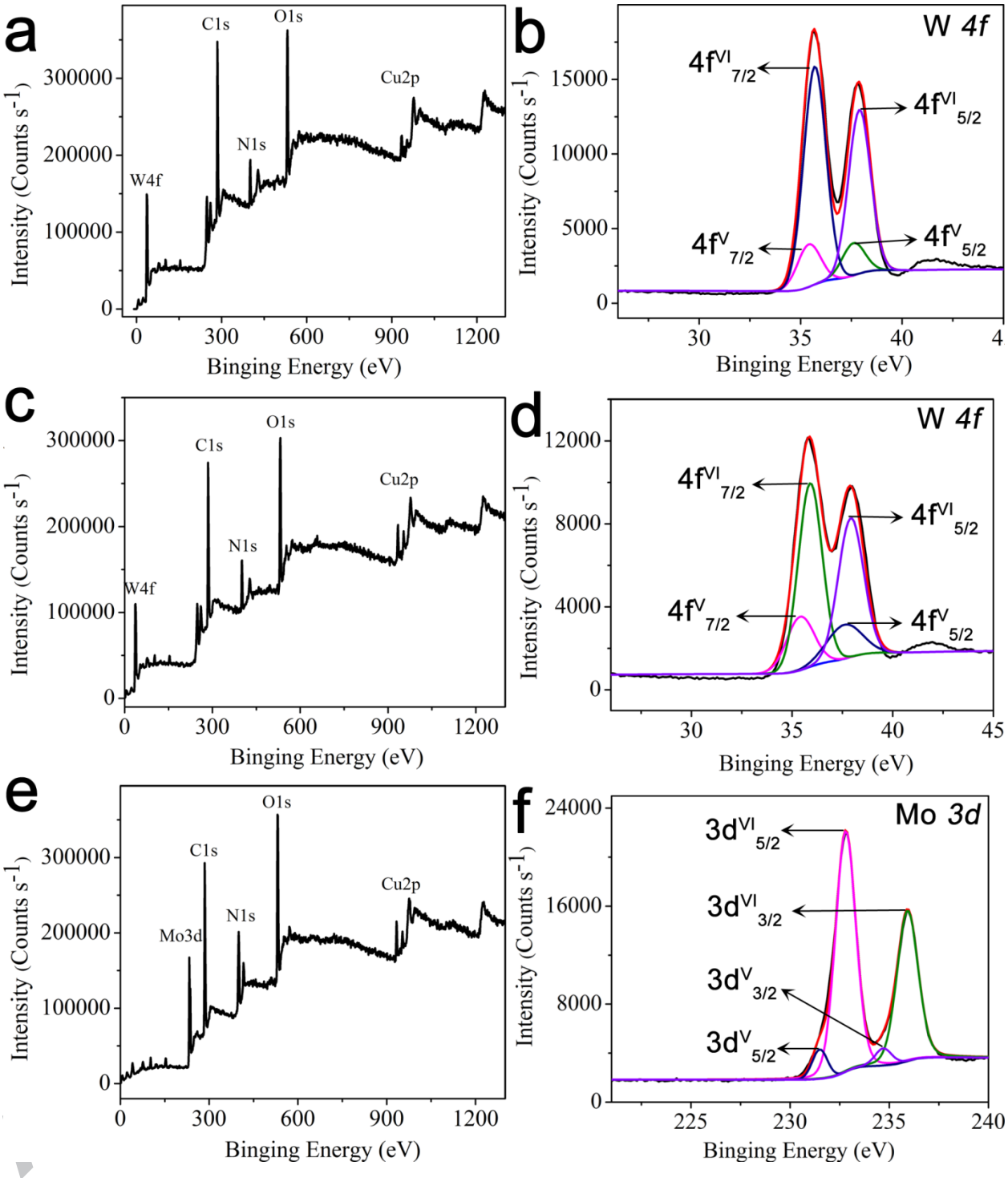

Figure 4. *XPS spectra of* ***2*** *(a),* ***3*** *(c) and* ***5*** *(e); XPS high-resolution for the W(4f) region in* ***2*** *(b) and* ***3*** *(d) and for the Mo(3d) region in* ***5*** *(f).*

2.5 Electrochemical performance. To explore the relationship between W-based POMOF structures and their capacitance performance, compounds **1**, **2** and **3** were used as electrode materials to measure the electrochemical performance in cyclic voltammetry (CV), galvanostatic charge/discharge (GCD) and electrochemical impedance spectroscopy (EIS).

As shown in Figures 5a to 5c, all the CV tests of PW_{12} series of compounds **1-3** were conducted in a potential window from -0.6 to 0.1 V *vs*. Ag/AgCl.[20] Obviously, in contrast to the rectangular CV curve shapes of normal electrical double-layer capacitor, the shapes of the CV curves of all the obtained electrodes with faradaic capacitive characteristics show reversible multiple pairs of redox peaks, which represents the redox processes of W centres in PW_{12} polyoxoanions.[86, 87] When the scan rate is increased, the shapes of the CV curves do not change significantly only showing an important change in the current intensity, which demonstrates a high rate capability.[88] The slight shifts of the redox peaks of these compounds could be attributed to the conductivity and thereby polarization of the electrodes.[89-91] Additionally, the observed linear relationship between the anodic and cathodic peak currents versus the scan rates from 5 to 100 mV s^{-1} (inset in Figures 5a-c) suggests that all these electrodes exhibit surface-controlled redox reactions,[92] which also proves that these compounds belong to capacitor-type materials rather than battery-type materials.[93] As shown in Figure 5d, the CV curve of **1** shows the largest integrated area among **1-3**, indicating a largest capacitance for **1**.

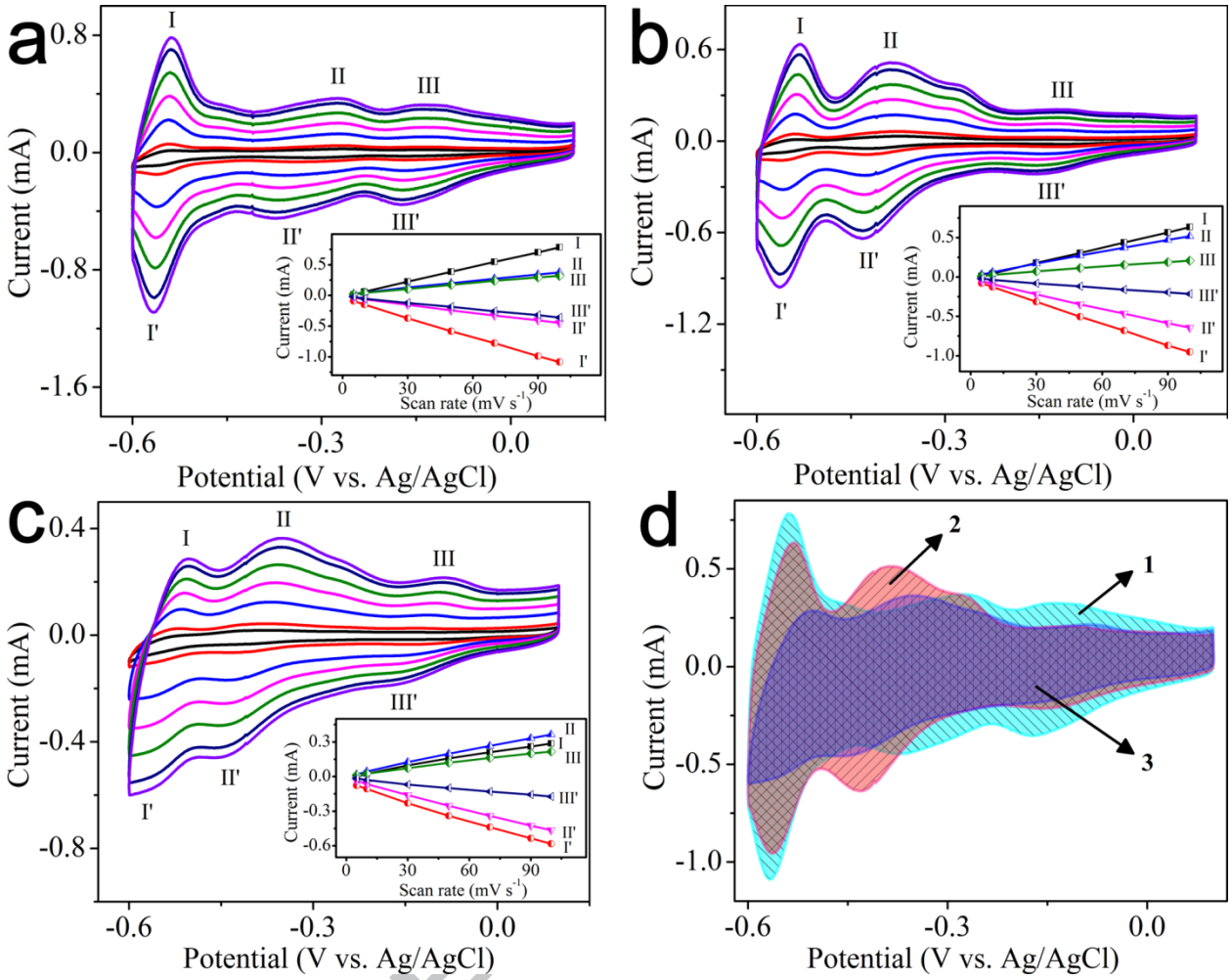

Figure 5. *CV curves of **1** (a), **2** (b) and **3** (c) based electrodes at 5, 10, 30, 50, 70, 90 and 100 mV s^{-1} (inset shows plots of the anodic and cathodic peak currents vs. scan rates); (d) CV curves of **1** (blue), **2** (red) and **3** (purple) at 100 mV s^{-1}.*

Figures 6a to 6c display the GCD curves of **1-3** at different current densities. Compound **1** shows the highest specific capacitance of 100.0, 84.8, 76.3, 71.4, 69.4, 66.4 and 64.3 F g^{-1} at the current densities of 2, 3, 5, 8, 10, 15 and 20 A g^{-1}, respectively.

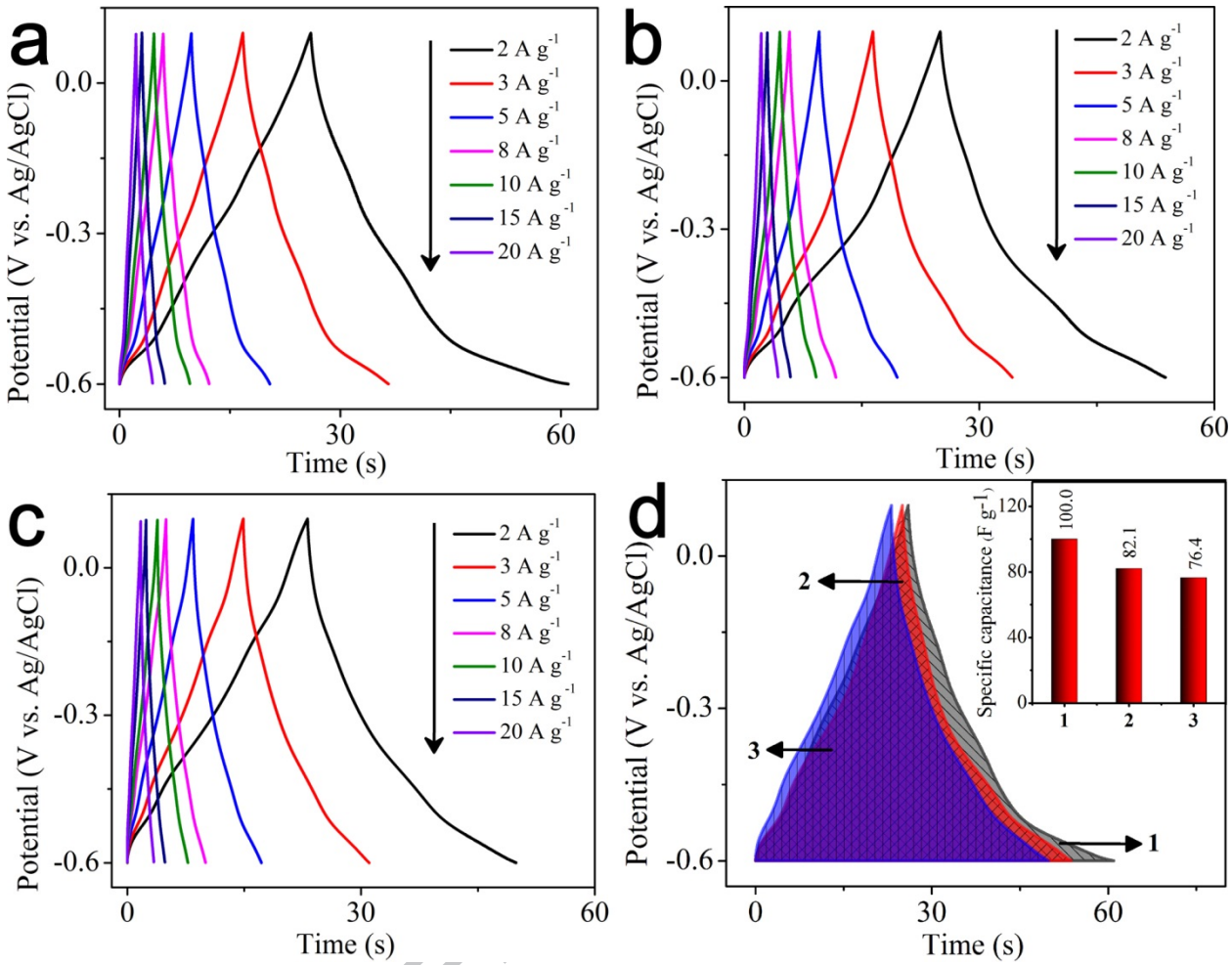

Figure 6. *GCD curves of **1** (a), **2** (b) and **3** (c) based electrodes at current densities of 2, 3, 5, 8, 10, 15 and 20 A g^{-1}; (d) GCD curves of **1** (blue), **2** (red) and **3** (purple) at 2 A g^{-1}. Inset shows the specific capacitance at a current density of 2 A g^{-1} for the three compounds.*

Figure 6d compares the capacitance of **1**-**3** at the same current density. As expected, the electrode of **1**-based exhibits the highest specific capacitance up to 100.0 F g^{-1} at 2 A g^{-1}, in agreement with the enclosed area in Figure 5d. This result may be attributed to the unique brick-wall like structure observed in **1** that provides an excellent electronic conductivity. In contrast, compounds **2** and **3** show 3D POMOF structures and, accordingly lower specific capacitance. The higher specific capacitance of compound **2** compared to **3** may be due to its 1D + 3D

pseudo-rotaxane structure, where the "strings" could provide additional electronic transmission paths compared to **3**.

In order to explore whether the capacitance are boosted by the increasing oxidation ability of Mo-based POMOFs compared to W-based POMOFs,[94] we have measured the electrochemical performance of compounds **4** and **5** under similar conditions to those of compounds **1-3**. As shown in Figures 7a and 7b, comparing with the potential window of compounds **1-3** (W-based POMOFs), the CV tests were conducted in a different potential window from -0.05 to 0.55 V for **4** (PMo_{12}-based POMOF) and -0.05 to 0.45 V *vs*. Ag/AgCl for **5** ($SiMo_{12}$-based POMOF).[20, 95] The shapes of the CV curves also suggest the redox processes of Mo centres in PMo_{12} or $SiMo_{12}$, polyoxoanions and faradaic capacitive characteristics.[86, 95] As observed in compounds **1-3**, the shapes of the CV curves do not change significantly when the scan rate is increased only showing an important change in the current intensity, which demonstrates high rate capability.[88] Additionally, as shown in Figure S11, compounds **4** and **5** also exhibit surface-controlled redox reactions with increasing scan rates from 5 to 100 mV s^{-1}.[92] Figures 7c and 7d display the charge/discharge curves of **4** and **5** at different current densities. The values of specific capacitance are 237.0, 230.5, 220.6, 212.9, 208.5, 200.8 and 193.3 F g^{-1} in compound **4**, and 138.4, 138.1, 135.7, 133.3, 132.6, 129.3 and 127.2 F g^{-1} in compound **5**, at the current densities of 2, 3, 5, 8, 10, 15 and 20 A g^{-1}, respectively. Remarkably, the specific capacitance of **4** and **5** are both higher than MoS_2–rGO/GCE (104 F g^{-1} at 4 A g^{-1}).[96] The result shows that the specific capacitance not only depends on the type of molybdenum source, but also on the microstructure. Moreover, the specific capacitance of compound **4** also could be comparable with state-of-the-art MOF-based and POM-based supercapacitor electrode materials, as listed in Table S7. When the current density is increased

from 2 to 20 A g^{-1}, a total of 74.2 % of the initial capacitance in **4** is retained, indicative of a good rate capability. As expected, the specific capacitance of the PMo_{12}-POMOF (compound **4**) is higher than that of the isostructural PW_{12}-POMOF (compound **1**), suggesting that the increasing oxidation ability of metal atoms in the Keggin POM improves the capacitance performance. The higher capacitance of the $SiMo_{12}$-POMOF (compound **5**) compared to the isostructural PW_{12}-POMOF (compound **2**), further confirms this effect. In addition, the results of the specific capacitance of both **1** and **5** are higher than **2**, which confirms that the capacitance of these POMOFs not only depends on the dimensionalities and microstructures of the POMOFs, but also on the types of POMs and their constituent metal atoms. The possible mechanism could be concluded as shown in Figure S12. Furthermore, if the operating voltage range of compounds **1** and **4** could be broadened in aqueous, they would be applied to ECs in future, and compounds **1** and **4** can be considered as negative and positive materials, respectively, or building asymmetric supercapacitor (ASC) directly.

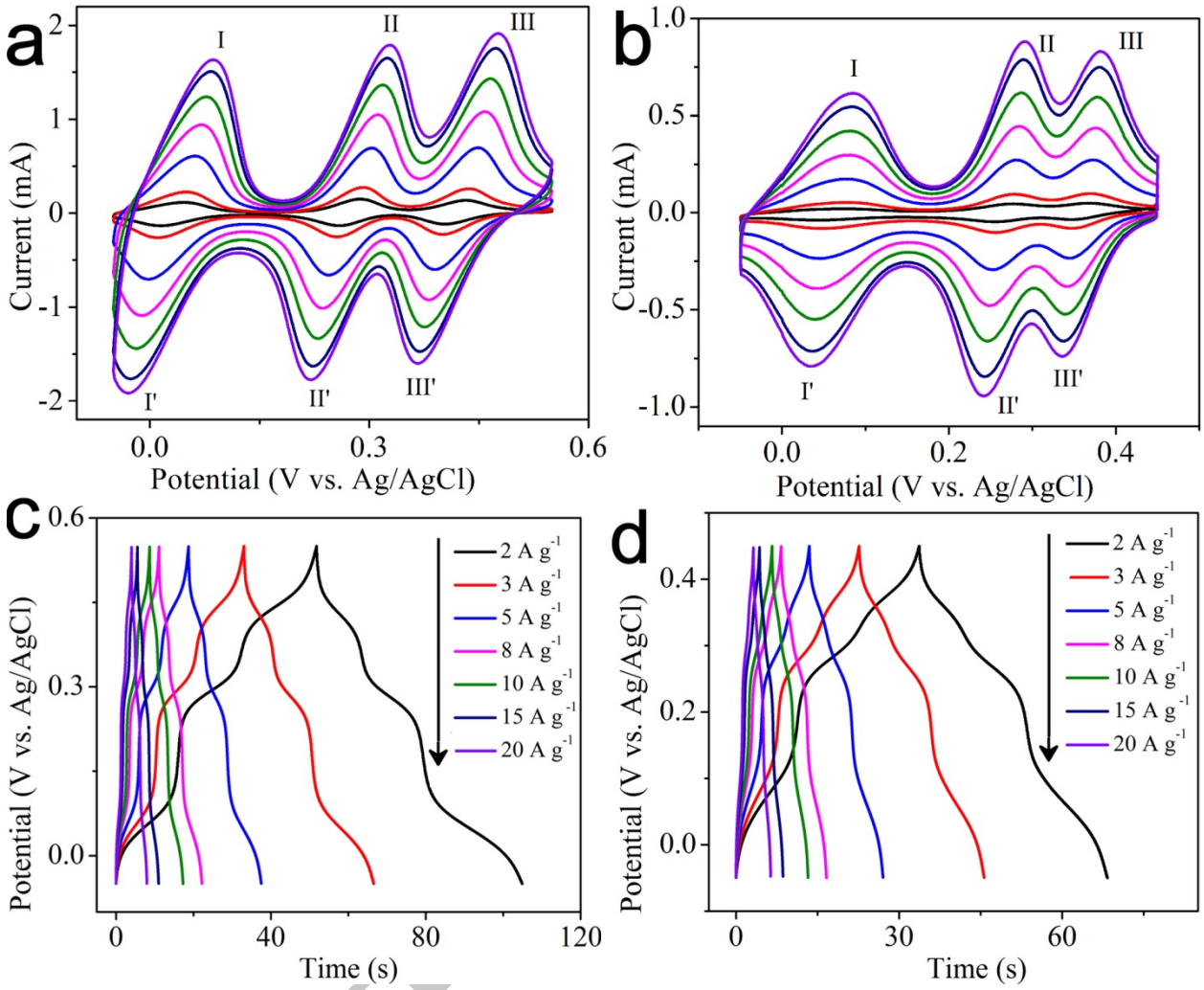

Figure 7. *CV curves of **4** (a) and **5** (b) based electrodes at 5, 10, 30, 50, 70, 90 and 100 mV s^{-1}; GCD curves of **4** (c) and **5** (d) based electrodes at current densities of 2, 3, 5, 8, 10, 15 and 20 A g^{-1}.*

To further characterize the electrochemical properties of compounds **1**-**5**, EIS measurements have been conducted, as shown in Figure 8a. The proposed equivalent circuit and corresponding values of R_c and R_{ct} of the electrodes have been calculated, as shown in Figure S13 and Table S8. The smallest intersection with the real axis shown by compound **4** at high frequency indicates that this electrode presents the lowest ohmic resistance of these compounds.[97-99]

Additionally, the largest slope in the low frequency region of **4**-based electrode indicates that this electrode shows the lowest ion diffusion resistance among all the as-prepared electrodes.[100-102] These results indicate that both factors, the special brick-wall like structures and the presence of Mo metal atoms with a higher oxidation ability, play positive roles for boosting the capacitance performance.

The cycling stabilities as electrochemical capacitor were evaluated by carrying out multiple charge/discharge cycles. As shown in Figures 8b and S14, all compounds show good cycling stabilities after 1000 cycles at a current density of 10 A g^{-1}, suggesting that the structures of compounds **1-5** remain stable during the charge/discharge processes. Additionally, the FT-IR spectra and SEM images before and after electrochemical measurements have been done to prove the stability of electrode materials, as shown in Figure S15 to S21. The good stability of title compounds could be attributed to their special POMOF structures. These POMOFs obtained in acidic solution and inner Keggin POMs possessing reversible multi-electron transfer reactions. The Keggin POMs possess many surface oxygen atoms with high negative charges that increase the template-scaffold interactions and the stability of the whole POMOF structures.

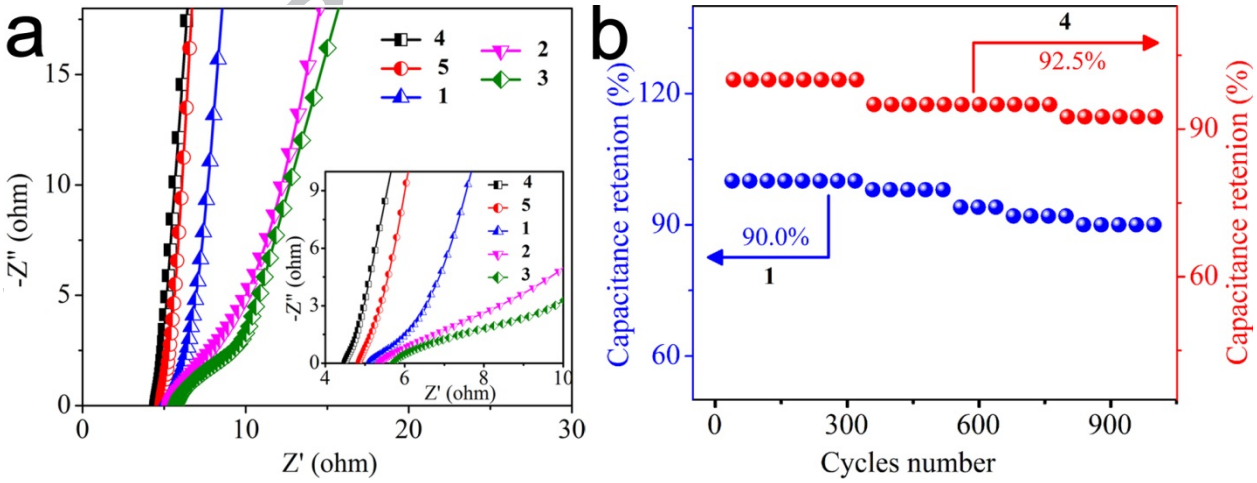

Figure 8. *(a) EIS spectra of **1** (blue), **2** (pink), **3** (green), **4** (black) and **5** (red) based electrodes (enlarged image as inset); (b) Cycling stabilities of **1** (blue sphere) and **4** (red sphere) based electrodes during 1000 cycles at the current density of 10 A g^{-1}.*

3. Conclusion

Five crystalline POMOFs have been synthesized with hydrothermal reactions: $[Cu^{I}_4H_2(btx)_5(PW_{12}O_{40})_2]\cdot 2H_2O$ (**1**), $[Cu^{II}Cu^{I}_3(H_2O)_2(btx)_5(PW^{VI}_{10}W^{V}_2O_{40})]\cdot 2H_2O$ (**2**), $[Cu^{I}_6(btx)_6(PW^{VI}_9W^{V}_3O_{40})]\cdot 2H_2O$ (**3**), $[Cu^{I}_4H_2(btx)_5(PMo_{12}O_{40})_2]\cdot 2H_2O$ (**4**) and $[Cu^{II}Cu^{I}_3(btx)_5(SiMo^{VI}_{11}Mo^{V}O_{40})]\cdot 4H_2O$ (**5**). Compounds **1** and **4** present layered structures formed by POMs and btx-Cu chains. Compounds **2** and **5** show a 1D + 3D *pseudo*-rotaxane structure with molecular "strings" formed by btx-Cu chains inserted into 3D molecular "loops" formed by btx, Cu ions and POMs. Compound **3** may be considered as a 3D open framework inserted by 2D guest sheets.

Compounds **1** and **4** are isostructural (as well as compounds **2** and **5**) and differ only in the composition of their Keggin POMs. On the other hand, the Keggin POMs in compounds **1-3** have the same composition (PW_{12}) although with different oxidation states: $(PW^{VI}_{12})^{3-}$ in **1**, $(PW^{VI}_{10}W^{V}_2)^{5-}$ in **2** and $(PW^{VI}_9W^{V}_3)^{6-}$ in **3** (table 1). Compounds **4** and **5** contain similar Keggin POMs (XMo_{12}) although with different oxidation states $(PMo^{VI}_{12})^{3-}$ in **4** and $(SiMo^{VI}_{11}Mo^{V})^{5-}$ in **5** (table 1).

Table 1. POM type, POMOF structure and capacitance performance at a current density of 2 A g^{-1} for compounds **1-5**.

Compound	POM type	POMOF structure	capacitance (F g^{-1})
1	$(PW^{VI}_{12}O_{40})^{3-}$	2D brick-wall like layer	100.0
2	$(PW^{VI}_{10}W^{V}_2O_{40})^{5-}$	1D + 3D *pseudo*-rotaxane	82.1

3	$(PW^{VI}_{9}W^{V}_{3}O_{40})^{6-}$	3D intersectant structure	76.4
4	$(PMo^{VI}_{12}O_{40})^{3-}$	2D brick-wall like layer	237.0
5	$(SiMo^{VI}_{11}Mo^{V})^{5-}$	1D + 3D *pseudo*-rotaxane	138.4

The analyses of the capacitance performance of compounds **1-5** (table 1) from their composition and oxidation states show three clear conclusions:

(1) Compounds **1** and **4**, where the metal atoms fully oxidized (W^{VI}_{12} in **1** and Mo^{VI}_{12} in **4**), show higher capacitance performance than their partially reduced derivatives ($W^{VI}_{10}W^{V}_{2}$ in **2**, $W^{VI}_{9}W^{V}_{3}$ in **3** and $Mo^{VI}_{11}Mo^{V}$ in **5**). This fact reflects the higher oxidation capacity of the fully oxidized Keggin POMs.

(2) Compounds **4** and **5**, containing Mo as metal atoms in the Keggin POM, show much higher capacitance performance than the corresponding W-containing POMs (compounds **1**-**3**). This fact agrees with the much higher oxidation capacity of Mo compared to W.

(3) All compounds show very high cycling stabilities with a retention of *ca*. 90 % of their capacitance performance after 1000 cycles.

Additionally, we are working in the syntheses of new POMOFs with unique microstructure and high oxidation capacity (mainly with Mo^{VI} ions) in order to improve the capacitance performance and applications in molecular electronics.

Acknowledgment

This work was financially supported by the National Science Foundation of China (21671049, 51572063 and 21701037). We also thank the NSF of Heilongjiang Province (LH2019B009), the Spanish MINECO (project CTQ2017-87201-P AEI/FEDER, EU) and the Generalitat Valenciana (project Prometeo II/2014/076) and the Fundamental Research Foundation for Universities of Heilongjiang Province (LGYC2018JQ007) for financial support.

Appendix A. Supplementary data

Supplementary data including crystal data of compounds **1-5** (cif) associated with this article can be found, in the online version, at http://dx.doi.org/10.1016/j.cej.xxxxxx. Syntheses process of title compounds, single crystal X-ray crystallography and structure refinement, preparation of the working electrodes, other figures of title compounds, some characterizations, additional electrochemical measurements, additional discussion including the morphologies of prepared electrodes and the mechanism for capacitance performance of title compounds are described in the supporting information.

ORCID

Dongfeng Chai: 0000-0002-7971-7391

Carlos J. Gómez-García: 0000-0002-0015-577X

Haijun Pang: 0000-0002-0405-8352

Huiyuan Ma: 0000-0002-2695-3243

References

[1] A.F.M. El-Mahdy, C. Young, J. Kim, J. You, Y. Yamauchi, S.-W. Kuo, Hollow Microspherical and Microtubular [3 + 3] Carbazole-Based Covalent Organic Frameworks and Their Gas and Energy Storage Applications, ACS Appl. Mater. Interfaces 11 (2019) 9343-9354.

[2] A.F.M. El-Mahdy, C.-H. Kuo, A. Alshehri, C. Young, Y. Yamauchi, J. Kim, S.-W. Kuo, Strategic design of triphenylamine- and triphenyltriazine-based two-dimensional covalent organic frameworks for CO_2 uptake and energy storage, J. Mater. Chem. A 6 (2018) 19532-19541.

[3] X. Zhao, W. Cai, Y. Yang, X. Song, Z. Neale, H.-E. Wang, J. Sui, G. Cao, $MoSe_2$ nanosheets perpendicularly grown on graphene with Mo–C bonding for sodium-ion capacitors, Nano Energy 47 (2018) 224-234.

[4] X. Li, J. Wei, Q. Li, S. Zheng, Y. Xu, P. Du, C. Chen, J. Zhao, H. Xue, Q. Xu, H. Pang, Nitrogen-Doped Cobalt Oxide Nanostructures Derived from Cobalt–Alanine Complexes for High-Performance Oxygen Evolution Reactions, Adv. Funct. Mater. 28 (2018) 1800886.

[5] Q. Li, L. Zhang, J. Dai, H. Tang, Q. Li, H. Xue, H. Pang, Polyoxometalate-based materials for advanced electrochemical energy conversion and storage, Chem. Eng. J. 351 (2018) 441-461.

[6] X. Zhao, H.-E. Wang, R.C. Massé, J. Cao, J. Sui, J. Li, W. Cai, G. Cao, Design of coherent anode materials with 0D Ni_3S_2 nanoparticles self-assembled on 3D interconnected carbon networks for fast and reversible sodium storage, J. Mater. Chem. A 5 (2017) 7394-7402.

[7] L. Zhang, S. Zheng, L. Wang, H. Tang, H. Xue, G. Wang, H. Pang, Fabrication of Metal Molybdate Micro/Nanomaterials for Electrochemical Energy Storage, Small 13 (2017) 1700917.

[8] X. Guo, S. Zheng, G. Zhang, X. Xiao, X. Li, Y. Xu, H. Xue, H. Pang, Nanostructured graphene-based materials for flexible energy storage, Energy Storage Materials 9 (2017) 150-169.

[9] J. Kim, C. Young, J. Lee, Y.-U. Heo, M.-S. Park, M.S.A. Hossain, Y. Yamauchi, J.H. Kim, Nanoarchitecture of MOF-derived nanoporous functional composites for hybrid supercapacitors, J. Mater. Chem. A 5 (2017) 15065-15072.

[10] J. Kim, J.H. Kim, K. Ariga, Redox-Active Polymers for Energy Storage Nanoarchitectonics, Joule 1 (2017) 739-768.

[11] J. Kim, C. Young, J. Lee, M.-S. Park, M. Shahabuddin, Y. Yamauchi, J.H. Kim, CNTs grown on nanoporous carbon from zeolitic imidazolate frameworks for supercapacitors, Chem. Commun. 52 (2016) 13016-13019.

[12] A. González, E. Goikolea, J.A. Barrena, R. Mysyk, Review on supercapacitors: Technologies and materials, Renew. Sust. Energ. Rev. 58 (2016) 1189-1206.

[13] Y. Ji, L. Huang, J. Hu, C. Streb, Y.-F. Song, Polyoxometalate-functionalized nanocarbon materials for energy conversion, energy storage and sensor systems, Energ. Environ. Sci. 8 (2015) 776-789.

[14] C. Xiaoli, Z. Ye, R.V.A. L., H. Su-Ting, Evolutionary Metal Oxide Clusters for Novel Applications: Toward High-Density Data Storage in Nonvolatile Memories, Adv. Mater. 30 (2018) 1703950.

[15] G. Bajwa, M. Genovese, K. Lian, Multilayer Polyoxometalates-Carbon Nanotube Composites for Electrochemical Capacitors, ECS J. Solid State Sc. 2 (2013) M3046-M3050.

[16] C.G. Lin, J. Hu, Y.F. Song, Polyoxometalate-Functionalized Nanocarbon Materials for Energy Conversion, Energy Storage, and Sensor Systems, Adv. Inorg. Chem. 69 (2017) 181-212.

[17] S. Park, K. Lian, Y. Gogotsi, Pseudocapacitive Behavior of Carbon Nanoparticles Modified by Phosphomolybdic Acid, J. Electrochem. Soc. 156 (2009) A921.

[18] L. Zhang, S. Li, C.J. Gómez-García, H. Ma, C. Zhang, H. Pang, B. Li, Two Novel Polyoxometalate-Encapsulated Metal–Organic Nanotube Frameworks as Stable and Highly Efficient Electrocatalysts for Hydrogen Evolution Reaction, ACS Appl. Mater. Interfaces 10 (2018) 31498-31504.

[19] F.M. Toma, A. Sartorel, M. Iurlo, M. Carraro, P. Parisse, C. Maccato, S. Rapino, B.R. Gonzalez, H. Amenitsch, T. Da Ros, L. Casalis, A. Goldoni, M. Marcaccio, G. Scorrano, G.

Scoles, F. Paolucci, M. Prato, M. Bonchio, Efficient water oxidation at carbon nanotube–polyoxometalate electrocatalytic interfaces, Nat. Chem. 2 (2010) 826-831.

[20] M. Sadakane, E. Steckhan, Electrochemical Properties of Polyoxometalates as Electrocatalysts, Chem. Rev. 98 (1998) 219-237.

[21] J.-S. Li, Y.-J. Tang, C.-H. Liu, S.-L. Li, R.-H. Li, L.-Z. Dong, Z.-H. Dai, J.-C. Bao, Y.-Q. Lan, Polyoxometalate-based metal–organic framework-derived hybrid electrocatalysts for highly efficient hydrogen evolution reaction, J. Mater. Chem. A 4 (2016) 1202-1207.

[22] S. Li, L. Zhang, B. Lu, E. Yan, T. Wang, L. Li, J. Wang, Y. Yu, Q. Mu, A new polyoxovanadate-based metal–organic framework: synthesis, structure and photo-/electro-catalytic properties, New J. Chem. 42 (2018) 7247-7253.

[23] S. Roy, V. Vemuri, S. Maiti, K.S. Manoj, U. Subbarao, S.C. Peter, Two Keggin-Based Isostructural POMOF Hybrids: Synthesis, Crystal Structure, and Catalytic Properties, Inorg. Chem. 57 (2018) 12078-12092.

[24] L. Ni, G. Yang, C. Sun, G. Niu, Z. Wu, C. Chen, X. Gong, C. Zhou, G. Zhao, J. Gu, W. Ji, X. Huo, M. Chen, G. Diao, Self-assembled three-dimensional graphene/polyaniline/polyoxometalate hybrid as cathode for improved rechargeable lithium ion batteries, Mater. Today Energy 6 (2017) 53-64.

[25] H. Yang, T. Song, L. Liu, A. Devadoss, F. Xia, H. Han, H. Park, W. Sigmund, K. Kwon, U. Paik, Polyaniline/Polyoxometalate Hybrid Nanofibers as Cathode for Lithium Ion Batteries with Improved Lithium Storage Capacity, J. Phys. Chem. C 117 (2013) 17376-17381.

[26] H. Wang, S. Hamanaka, Y. Nishimoto, S. Irle, T. Yokoyama, H. Yoshikawa, K. Awaga, In Operando X-ray Absorption Fine Structure Studies of Polyoxometalate Molecular Cluster Batteries: Polyoxometalates as Electron Sponges, J. Am. Chem. Soc. 134 (2012) 4918-4924.

[27] D.P. Dubal, N.R. Chodankar, A. Vinu, D.H. Kim, P. Gomez-Romero, Asymmetric Supercapacitors Based on Reduced Graphene Oxide with Different Polyoxometalates as Positive and Negative Electrodes, ChemSusChem 10 (2017) 2742-2750.

[28] M. Genovese, K. Lian, Polyoxometalate modified pine cone biochar carbon for supercapacitor electrodes, J. Mater. Chem. A 5 (2017) 3939-3947.

[29] M. Genovese, K. Lian, Ionic Liquid-Derived Imidazolium Cation Linkers for the Layer-by-Layer Assembly of Polyoxometalate-MWCNT Composite Electrodes with High Power Capability, ACS Appl. Mater. Interfaces 8 (2016) 19100-19109.

[30] D.P. Dubal, J. Suarez-Guevara, D. Tonti, E. Enciso, P. Gomez-Romero, A high voltage solid state symmetric supercapacitor based on graphene–polyoxometalate hybrid electrodes with a hydroquinone doped hybrid gel-electrolyte, J. Mater. Chem. A 3 (2015) 23483-23492.

[31] Y.-Q. Lan, Polypyrrole-polyoxometalate/reduced graphene oxide ternary nanohybrids for flexible, all-solid-state supercapacitors, Chem. Commun. 51 (2015) 12377.

[32] R. Li, C. He, L. Cheng, G. Lin, G. Wang, D. Shi, R.K.-Y. Li, Y. Yang, Polyoxometalate-enabled photoreduction of graphene oxide to bioinspired nacre-like composite films for supercapacitor electrodes, Compos. Part B-Eng. 121 (2017) 75-82.

[33] S. Herrmann, N. Aydemir, F. Nägele, D. Fantauzzi, T. Jacob, J. Travas-Sejdic, C. Streb, Enhanced Capacitive Energy Storage in Polyoxometalate-Doped Polypyrrole, Adv. Funct. Mater. 27 (2017) 1700881.

[34] Z. Jovanović, I. Holclajtner-Antunović, D. Bajuk-Bogdanović, S. Jovanović, Ž. Mravik, M. Vujković, Effect of thermal treatment on the charge storage properties of graphene oxide/12-tungstophosphoric acid nanocomposite, Electrochem. Commun. 83 (2017) 36-40.

[35] M. Yang, S.B. Hong, J.H. Yoon, D.S. Kim, S.W. Jeong, D.E. Yoo, T.J. Lee, K.G. Lee, S.J. Lee, B.G. Choi, Fabrication of Flexible, Redoxable, and Conductive Nanopillar Arrays with Enhanced Electrochemical Performance, ACS Appl. Mater. Interfaces 8 (2016) 22220-22226.

[36] S. Herrmann, C. Ritchie, C. Streb, Polyoxometalate-conductive polymer composites for energy conversion, energy storage and nanostructured sensors, Dalton transactions 44 (2015) 7092-7104.

[37] M. Yang, B.G. Choi, S.C. Jung, Y.-K. Han, Y.S. Huh, S.B. Lee, Polyoxometalate-coupled Graphene via Polymeric Ionic Liquid Linker for Supercapacitors, Adv. Funct. Mater. 24 (2014) 7301-7309.

[38] M. Sosnowska, M. Goral-Kurbiel, M. Skunik-Nuckowska, R. Jurczakowski, P.J. Kulesza, Hybrid materials utilizing polyelectrolyte-derivatized carbon nanotubes and vanadium-mixed addenda heteropolytungstate for efficient electrochemical charging and electrocatalysis, J. Solid State Electr. 17 (2013) 1631-1640.

[39] Z. Cui, C.X. Guo, W. Yuan, C.M. Li, In situ synthesized heteropoly acid/polyaniline/graphene nanocomposites to simultaneously boost both double layer- and pseudo-capacitance for supercapacitors, Phys. Chem. Chem. Phys. 14 (2012) 12823-12828.

[40] G.M. Suppes, C.G. Cameron, M.S. Freund, A Polypyrrole/Phosphomolybdic Acid | Poly(3,4-ethylenedioxythiophene)/Phosphotungstic Acid Asymmetric Supercapacitor, J. Electrochem. Soc. 157 (2010) A1030-A1034.

[41] A.M. White, R.C.T. Slade, Investigation of vapour-grown conductive polymer/heteropolyacid electrodes, Electrochim. Acta 48 (2003) 2583-2588.

[42] D.P. Dubal, B. Ballesteros, A.A. Mohite, P. Gomez-Romero, Functionalization of Polypyrrole Nanopipes with Redox-Active Polyoxometalates for High Energy Density Supercapacitors, ChemSusChem 10 (2017) 731-737.

[43] A. Guillén-López, N.D. Espinosa-Torres, A.K. Cuentas-Gallegos, M. Robles, J. Muñiz, Understanding bond formation and its impact on the capacitive properties of SiW12 polyoxometalates adsorbed on functionalized carbon nanotubes, Carbon 130 (2018) 623-635.

[44] N. Campagnol, R. Romero-Vara, W. Deleu, L. Stappers, K. Binnemans, D.E. De Vos, J. Fransaer, A Hybrid Supercapacitor based on Porous Carbon and the Metal-Organic Framework MIL-100(Fe), ChemElectroChem 1 (2014) 1182-1188.

[45] L. Wang, X. Feng, L. Ren, Q. Piao, J. Zhong, Y. Wang, H. Li, Y. Chen, B. Wang, Flexible Solid-State Supercapacitor Based on a Metal–Organic Framework Interwoven by Electrochemically-Deposited PANI, J. Am. Chem. Soc. 137 (2015) 4920-4923.

[46] Y. Yan, Y. Luo, J. Ma, B. Li, H. Xue, H. Pang, Facile Synthesis of Vanadium Metal-Organic Frameworks for High-Performance Supercapacitors, Small 14 (2018) 1801815.

[47] C. Young, J. Kim, Y.V. Kaneti, Y. Yamauchi, One-Step Synthetic Strategy of Hybrid Materials from Bimetallic Metal–Organic Frameworks for Supercapacitor Applications, ACS Appl. Energy Mater. 1 (2018) 2007-2015.

[48] G. Xu, P. Nie, H. Dou, B. Ding, L. Li, X. Zhang, Exploring metal organic frameworks for energy storage in batteries and supercapacitors, Mater. Today 20 (2017) 191-209.

[49] R.R. Salunkhe, Y.V. Kaneti, J. Kim, J.H. Kim, Y. Yamauchi, Nanoarchitectures for Metal–Organic Framework-Derived Nanoporous Carbons toward Supercapacitor Applications, Accounts Chem. Res. 49 (2016) 2796-2806.

[50] C. Wang, C. Liu, J. Li, X. Sun, J. Shen, W. Han, L. Wang, Electrospun metal–organic framework derived hierarchical carbon nanofibers with high performance for supercapacitors, Chem. Commun. 53 (2017) 1751-1754.

[51] C. Wang, Y.V. Kaneti, Y. Bando, J. Lin, C. Liu, J. Li, Y. Yamauchi, Metal–organic framework-derived one-dimensional porous or hollow carbon-based nanofibers for energy storage and conversion, Mater. Horiz. 5 (2018) 394-407.

[52] J. Shao, J. Feng, H. Zhou, A. Yuan, Graphene aerogel encapsulated Fe-Co oxide nanocubes derived from Prussian blue analogue as integrated anode with enhanced Li-ion storage properties, Appl. Surf. Sci. 471 (2019) 745-752.

[53] K. Zhang, H. Yang, M. Lü, C. Yan, H. Wu, A. Yuan, S. Lin, Porous MoO_2-Cu/C/Graphene nano-octahedrons quadruple nanocomposites as an advanced anode for lithium ion batteries with enhanced rate capability, J. Alloy. Compd. 731 (2018) 646-654.

[54] J. Feng, H. Zhou, J. Wang, T. Bian, J. Shao, A. Yuan, MoS_2 supported on MOF-derived carbon with core-shell structure as efficient electrocatalysts for hydrogen evolution reaction, Int. J. Hydrogen Energ. 43 (2018) 20538-20545.

[55] R. Ramachandran, K. Rajavel, W. Xuan, D. Lin, F. Wang, Influence of $Ti3C_2T_x$ (MXene) intercalation pseudocapacitance on electrochemical performance of Co-MOF binder-free electrode, Ceram. Int. 44 (2018) 14425-14431.

[56] Y. Zhang, B. Lin, J. Wang, P. Han, T. Xu, Y. Sun, X. Zhang, H. Yang, Polyoxometalates@Metal-Organic Frameworks Derived Porous MoO_3@CuO as Electrodes for Symmetric All-Solid-State Supercapacitor, Electrochim. Acta 191 (2016) 795-804.

[57] G. Xia, D. Liu, F. Zheng, Y. Yang, J. Su, Q. Chen, Preparation of porous MoO_2@C nano-octahedrons from a polyoxometalate-based metal–organic framework for highly reversible lithium storage, J. Mater. Chem. A 4 (2016) 12434-12441.

[58] Q. Cheng, K. Tao, X. Han, Y. Yang, Z. Yang, Q. Ma, L. Han, Ultrathin Ni-MOF nanosheet arrays grown on polyaniline decorated Ni foam as an advanced electrode for asymmetric supercapacitors with high energy density, Dalton transactions 48 (2019) 4119-4123.

[59] Y.-L. Li, J.-J. Zhou, M.-K. Wu, C. Chen, K. Tao, F.-Y. Yi, L. Han, Hierarchical Two-Dimensional Conductive Metal–Organic Framework/Layered Double Hydroxide Nanoarray for a High-Performance Supercapacitor, Inorg. Chem. 57 (2018) 6202-6205.

[60] S. Zheng, B. Li, Y. Tang, Q. Li, H. Xue, H. Pang, Ultrathin nanosheet-assembled $[Ni_3(OH)_2(PTA)_2(H_2O)4]\cdot 2H_2O$ hierarchical flowers for high-performance electrocatalysis of glucose oxidation reactions, Nanoscale 10 (2018) 13270-13276.

[61] R. Ramachandran, W. Xuan, C. Zhao, X. Leng, D. Sun, D. Luo, F. Wang, Enhanced electrochemical properties of cerium metal-organic framework based composite electrodes for high-performance supercapacitor application, RSC Adv. 8 (2018) 3462-3469.

[62] Y. Xu, Q. Li, H. Xue, H. Pang, Metal-organic frameworks for direct electrochemical applications, Coordin. Chem. Rev. 376 (2018) 292-318.

[63] Y. Xu, B. Li, S. Zheng, P. Wu, J. Zhan, H. Xue, Q. Xu, H. Pang, Ultrathin two-dimensional cobalt-organic framework nanosheets for high-performance electrocatalytic oxygen evolution, J. Mater. Chem. A 6 (2018) 22070-22076.

[64] Q. Li, Y. Xu, S. Zheng, X. Guo, H. Xue, H. Pang, Recent Progress in Some Amorphous Materials for Supercapacitors, Small 14 (2018) 1800426.

[65] L. Li, R. Chen, Y. Gong, C. Yu, Z. Hui, H. Xu, X. Zhao, Y. Sun, W. Zhao, G. Sun, W. Huang, Assembling laminated films via the synchronous reduction of graphene oxide and formation of copper-based metal organic frameworks, J. Mater. Chem. A 7 (2019) 107-111.

[66] R. Ramachandran, C. Zhao, D. Luo, K. Wang, F. Wang, Synthesis of copper benzene-1, 3, 5-tricarboxylate metal organic frameworks with mixed phases as the electrode material for supercapacitor applications, Appl. Surf. Sci. 460 (2018) 33-39.

[67] Y. Gong, R. Chen, H. Xu, C. Yu, X. Zhao, Y. Sun, Z. Hui, J. Zhou, J. An, Z. Du, G. Sun, W. Huang, Polarity-assisted formation of hollow-frame sheathed nitrogen-doped nanofibrous carbon for supercapacitors, Nanoscale 11 (2019) 2492-2500.

[68] K. Rui, X. Wang, M. Du, Y. Zhang, Q. Wang, Z. Ma, Q. Zhang, D. Li, X. Huang, G. Sun, J. Zhu, W. Huang, Dual-Function Metal-Organic Framework-Based Wearable Fibers for Gas Probing and Energy Storage, ACS Appl. Mater. Interfaces 10 (2018) 2837-2842.

[69] L. Hua, Z. Hui, Y. Sun, X. Zhao, H. Xu, Y. Gong, R. Chen, C. Yu, J. Zhou, G. Sun, W. Huang, Oxygen vacancy enriched hollow cobaltosic oxide frames with ultrathin walls for efficient energy storage and biosensing, Nanoscale 10 (2018) 21006-21012.

[70] D. Chai, Y. Hou, K.P. O'Halloran, H. Pang, H. Ma, G. Wang, X. Wang, Enhancing Energy Storage via TEA-Dependent Controlled Syntheses: Two Series of Polyoxometalate-Based Inorganic-Organic Hybrids and their Supercapacitor Properties, ChemElectroChem 5 (2018) 3443-3450.

[71] G. Wang, T. Chen, S. Li, H. Pang, H. Ma, A coordination polymer based on dinuclear (pyrazinyl tetrazolate) copper(ii) cations and Wells-Dawson anions for high-performance supercapacitor electrodes, Dalton transactions 46 (2017) 13897-13902.

[72] G. Wang, T. Chen, X. Wang, H. Ma, H. Pang, High-Performance Supercapacitor Afforded by a High-Connected Keggin-Based 3D Coordination Polymer, Eur. J. Inorg. Chem. 2017 (2017) 5350-5355.

[73] R. Ramachandran, C. Zhao, D. Luo, K. Wang, F. Wang, Morphology-dependent electrochemical properties of cobalt-based metal organic frameworks for supercapacitor electrode materials, Electrochim. Acta 267 (2018) 170-180.

[74] J. Liang, Z. Liang, R. Zou, Y. Zhao, Heterogeneous Catalysis in Zeolites, Mesoporous Silica, and Metal–Organic Frameworks, Adv. Mater. 29 (2017) 1701139.

[75] H.T. Evans, M.T. Popev, Reinterpretation of five recent crystal structures of heteropoly and isopoly complexes: divanadodecamolybdophosphate, trivanadoenneamolybdophosphate, ".gamma.-dodecatungstophosphate", the dodecamolybdate-dodecamolybdomolybdate blue complex, and dihydrogen decavanadate, Inorg. Chem. 23 (1984) 501-504.

[76] P. Le Magueres, L. Ouahab, S. Golhen, D. Grandjean, O. Pena, J.C. Jegaden, C.J. Gomez-Garcia, P. Delhaes, Diamagnetic and Paramagnetic Keggin Polyoxometalate Salts Containing 1-D and 3-D decamethylferrocenium Networks: Preparation, Crystal Structures and Magnetic Properties of $[Fe(C_5Me_5)_2]_4(POM)(solv)n$ (POM = $[SiMo_{12}O_{40}]^{4-}$, $[SiW_{12}O_{40}]^{4-}$, $[PMo_{12}O_{40}]^{4-}$, $[HFeW_{12}O_{40}]^{4-}$; solv = H_2O, C_3H_7ON, CH_3CN), Inorg. Chem. 33 (1994) 5180-5187.

[77] C.J. Gómez-García, L. Ouahab, C. Gimenez-Saiz, S. Triki, E. Coronado, P. Delhaès, Coexistence of Mobile and Localized Electrons in Bis(ethylene)dithiotetrathiafulvalene (BEDT-TTF) Radical Salts with Paramagnetic Polyoxometalates: Synthesis and Physical Properties of $(BEDT\text{-}TTF)_8[CoW_{12}O_{40}]\cdot 5.5H_2O$, Angew. Chem. Int. Ed. 33 (1994) 223-226.

[78] C.J. Gomez-Garcia, C. Gimenez-Saiz, S. Triki, E. Coronado, P. Le Magueres, L. Ouahab, L. Ducasse, C. Sourisseau, P. Delhaes, Coexistence of Magnetic and Delocalized Electrons in

Hybrid Molecular Materials. The Series of Organic-Inorganic Radical Salts (BEDT-TTF)$_8$[$XW_{12}O_{40}$](solv)$_n$ (X = 2(H^+), B^{III}, Si^{IV}, Cu^{II}, Co^{II}, and Fe^{III}; solv = H_2O, CH_3CN), Inorg. Chem. 34 (1995) 4139-4151.

[79] E. Coronado, C.J. Gómez-García, Polyoxometalate-Based Molecular Materials, Chem. Rev. 98 (1998) 273-296.

[80] E. Coronado, J.R. Galán-Mascarós, C. Giménez-Saiz, C.J. Gómez-García, S. Triki, Hybrid Molecular Materials Based upon Magnetic Polyoxometalates and Organic π-Electron Donors: Syntheses, Structures, and Properties of Bis(ethylenedithio)tetrathiafulvalene Radical Salts with Monosubstituted Keggin Polyoxoanions, J. Am. Chem. Soc. 120 (1998) 4671-4681.

[81] E. Coronado, J. R. Galán-mascarós, C. Giménez-saiz, C. J. Gómez-garcía, C. Rovira, J. Tarrés, S. Triki, J. Veciana, Radical salts of the organic donor BET-TTF with polyoxometalate clusters, J. Mater. Chem. 8 (1998) 313-317.

[82] E. Coronado, J.R. Galán-Mascarós, C. Giménez-Saiz, C.J. Gómez-García, L.R. Falvello, P. Delhaès, Charge Transfer Salts Based on Polyoxometalates and Seleno-Substituted Organic Donors. Synthesis, Structure, and Magnetic Properties of (BEST)$_3$H[$PMo_{12}O_{40}$]·CH_3CN·CH_2Cl_2 (BEST = Bis(ethylenediseleno)tetrathiafulvalene), Inorg. Chem. 37 (1998) 2183-2188.

[83] X. Wang, Y. Bi, B. Chen, H. Lin, G. Liu, Self-Assembly of Organic–Inorganic Hybrid Materials Constructed from Eight-Connected Coordination Polymer Hosts with Nanotube Channels and Polyoxometalate Guests As Templates, Inorg. Chem. 47 (2008) 2442-2448.

[84] H. Seenivasan, P. Bera, J.N. Balaraju, K.S. Rajam, XPS Characterization and Microhardness of Heat Treated Co-W Coatings Electrodeposited with Gluconate Bath, Adv. Sci. Focus 1 (2013) 262-268.

[85] W. Jing, Z. Guang-Jin, Y. Wen-Sheng, Y. Jian-Nian, Multicolor Photochromism of Polymolybdate-Citric Acid Composite Films, Chinese J. Chem. 23 (2005) 1037-1041.

[86] J. Lin, H. Jia, H. Liang, S. Chen, Y. Cai, J. Qi, C. Qu, J. Cao, W. Fei, J. Feng, Hierarchical $CuCo_2S_4$@NiMn-layered double hydroxide core-shell hybrid arrays as electrodes for supercapacitors, Chem. Eng. J. 336 (2018) 562-569.

[87] D. Martel, M. Gross, Electrochemical study of multilayer films built on glassy carbon electrode with polyoxometalate anions and two multi-charged molecular cationic species, J. Solid State Electr. 11 (2007) 421-429.

[88] W. Fu, Y. Wang, W. Han, Z. Zhang, H. Zha, E. Xie, Construction of hierarchical $ZnCo_2O_4$@$Ni_xCo_{2x}(OH)_{6x}$ core/shell nanowire arrays for high-performance supercapacitors, J. Mater. Chem. A 4 (2016) 173-182.

[89] D. Guo, X. Song, L. Tan, H. Ma, W. Sun, H. Pang, L. Zhang, X. Wang, A facile dissolved and reassembled strategy towards sandwich-like rGO@NiCoAl-LDHs with excellent supercapacitor performance, Chem. Eng. J. 356 (2019) 955-963.

[90] R. Tummala, R.K. Guduru, P.S. Mohanty, Nanostructured Co_3O_4 electrodes for supercapacitor applications from plasma spray technique, J. Power Sources 209 (2012) 44-51.

[91] D. Guo, X. Song, F. Li, L. Tan, H. Ma, L. Zhang, Y. Zhao, Oriented synthesis of Co_3O_4 core-shell microspheres for high-performance asymmetric supercapacitor, Colloid. Surface. A 546 (2018) 1-8.

[92] G. Li, L. Anderson, Y. Chen, M. Pan, P.-Y. Abel Chuang, New insights into evaluating catalyst activity and stability for oxygen evolution reactions in alkaline media, Sustain. Energ. Fuels 2 (2018) 237-251.

[93] Y. Gogotsi, R.M. Penner, Energy Storage in Nanomaterials – Capacitive, Pseudocapacitive, or Battery-like?, ACS Nano 12 (2018) 2081-2083.

[94] I.V. Kozhevnikov, K.I. Matveev, Homogeneous catalysts based on heteropoly acids (review), Appl. Catal. 5 (1983) 135-150.

[95] T. Akter, K. Hu, K. Lian, Investigations of multilayer polyoxometalates-modified carbon nanotubes for electrochemical capacitors, Electrochim. Acta 56 (2011) 4966-4971.

[96] M. Saraf, K. Natarajan, S.M. Mobin, Emerging Robust Heterostructure of MoS_2–rGO for High-Performance Supercapacitors, ACS Appl. Mater. Interfaces 10 (2018) 16588-16595.

[97] F. Lu, M. Zhou, W. Li, Q. Weng, C. Li, Y. Xue, X. Jiang, X. Zeng, Y. Bando, D. Golberg, Engineering sulfur vacancies and impurities in $NiCo_2S_4$ nanostructures toward optimal supercapacitive performance, Nano Energy 26 (2016) 313-323.

[98] Y. Tang, T. Chen, S. Yu, Y. Qiao, S. Mu, S. Zhang, Y. Zhao, L. Hou, W. Huang, F. Gao, A highly electronic conductive cobalt nickel sulphide dendrite/quasi-spherical nanocomposite for a supercapacitor electrode with ultrahigh areal specific capacitance, J. Power Sources 295 (2015) 314-322.

[99] H. Niu, X. Yang, H. Jiang, D. Zhou, X. Li, T. Zhang, J. Liu, Q. Wang, F. Qu, Hierarchical core–shell heterostructure of porous carbon nanofiber@$ZnCo_2O_4$ nanoneedle arrays: advanced binder-free electrodes for all-solid-state supercapacitors, J. Mater. Chem. A 3 (2015) 24082-24094.

[100] J.L. Qi, J.H. Lin, X. Wang, J.L. Guo, L.F. Xue, J.C. Feng, W.-D. Fei, Low resistance VFG-Microporous hybrid Al-based electrodes for supercapacitors, Nano Energy 26 (2016) 657-667.

[101] X. Li, J. Rong, B. Wei, Electrochemical Behavior of Single-Walled Carbon Nanotube Supercapacitors under Compressive Stress, ACS Nano 4 (2010) 6039-6049.

[102] T. Liu, L. Finn, M. Yu, H. Wang, T. Zhai, X. Lu, Y. Tong, Y. Li, Polyaniline and Polypyrrole Pseudocapacitor Electrodes with Excellent Cycling Stability, Nano Letters 14 (2014) 2522-2527.

Highlights

- Integrating POMs with MOFs to construct stable and versatile POMOFs
- Five novel crystalline POMOFs are innovatively employed as capacitor materials
- The capacitance of POMOF electrodes is higher than traditional POM ones
- Tuning SAS is an effective method to boost the capacitance of POMOFs
- Obtaining a brick-wall like POMOF with large ECSA for high performance capacitance